

Article

Multi-Mission Satellite Detection and Tracking of October 2019 Sabiti Oil Spill in the Red Sea

Koteswararao Vankayalapati ¹, Hari Prasad Dasari ¹, Sabique Langodan ^{1,2}, Samah El Mohtar ¹, Sivareddy Sanikommu ¹, Khaled Asfahani ², Srinivas Desamsetti ^{1,3} and Ibrahim Hoteit ^{1,*}

¹ Physical Sciences and Engineering Division, King Abdullah University of Science and Technology, Thuwal 23955, Saudi Arabia

² Environmental Protection Department, Saudi Aramco, Dhahran 31261, Saudi Arabia

³ National Center for Medium Range Weather Forecasting, Noida 201301, India

* Correspondence: ibrahim.hoteit@kaust.edu.sa

Abstract: A multi-mission satellite remote sensing (MSRS) approach is explored to detect and track leaked oil from the Sabiti oil tanker accident that occurred in the central Red Sea on 11 October 2019 (RSOS-2019). The spilled oil spread rapidly and reached the coastal land near Jeddah, the second largest city of KSA, on 17 October. Different oil spill detection algorithms were implemented on SAR and optical sensor-based satellite images to track the oil spill. Sentinel-1 SAR images were most efficient at detecting the spread and thickness of RSOS-2019, but their spatio-temporal coverage greatly limits their use for tracking the oil movement. The spread and propagation of oil were well captured by Sentinel-2 images up to three weeks after the accident day, in agreement with the SAR images. MODIS successfully detected the narrow patch of oil that was leaked on the incident day and the widespread oil patches two days after. Landsat-8 RGB composite and thermal infrared images captured the oil spill on 13 October. By filtering clouds from the Meteosat images through sequential analysis, the spread and movement of the oil patches were efficiently tracked on 13 October. PlanetScope images available between 12 and 17 October enabled tracking of the oil near the coastal waters. The inferred oil spill movements are consistent with the ocean currents as revealed by a high-resolution regional ocean reanalysis. Our results demonstrate the potential of the MSRS approach to detect and track oil spills in the open and coastal waters of the Red Sea in near real-time.



Citation: Vankayalapati, K.; Dasari, H.P.; Langodan, S.; El Mohtar, S.; Sanikommu, S.; Asfahani, K.; Desamsetti, S.; Hoteit, I.

Multi-Mission Satellite Detection and Tracking of October 2019 Sabiti Oil Spill in the Red Sea. *Remote Sens.*

2023, 15, 38. <https://doi.org/10.3390/rs15010038>

Academic Editor: Huaqiang Du

Received: 12 October 2022

Accepted: 27 November 2022

Published: 22 December 2022



Copyright: © 2022 by the authors. Licensee MDPI, Basel, Switzerland. This article is an open access article distributed under the terms and conditions of the Creative Commons Attribution (CC BY) license (<https://creativecommons.org/licenses/by/4.0/>).

1. Introduction

Oil spills have adverse effects on the marine environment [1,2]. Oil tanker accidents are major sources of oil pollution, having resulted in approximately 5.86 million tons of oil being spilled globally to date [3,4].

The Red Sea has an average width of 280 km, length of 2000 km, and maximum depth exceeding 2500 m along its axial trench (Figure 1). It contributes approximately 10–20% of the GDP of the Kingdom of Saudi Arabia (KSA) [5]. The Red Sea basin is the main navigation route between east and west and has become one of the most important commercial pathways for maritime shipping and transport of crude oil from the oil-rich Arabian region [6]. Considering the massive transport of oil through its basin, the Red Sea is at great risk of potential oil spills; for example, more than 187 million tons of oil products crossed the Suez Canal in 2016 alone.

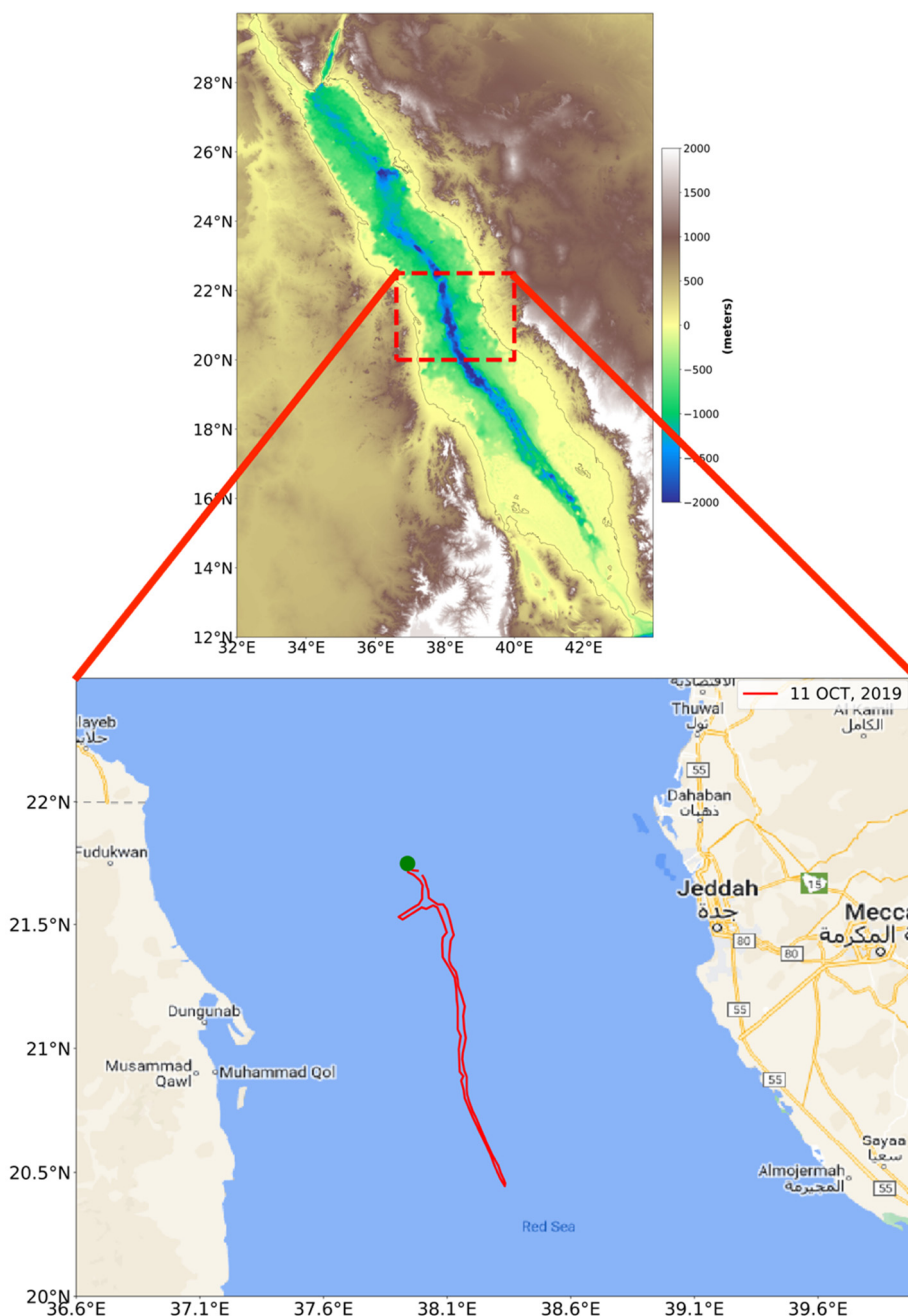


Figure 1. Topography map of the study area in the Red Sea (**top**). The green dot in the zoomed images (**bottom**) indicates the location of the oil leak on 11 October 2019, and the red line indicates the extent of the oil spilled from the Sabiti oil tanker.

The spread of an oil spill on the sea surface significantly depends on the physical and chemical properties of the ocean water, including viscosity, density, surface tension, and elasticity [7]. The dynamics of an oil spill are governed by various processes, such as spreading, evaporation, emulsification, and dispersion [7]. These processes, in turn, depend on the oil type, thickness, and ocean and weather conditions [7]. The natural dispersion rate of oil under moderate wind speed is approximately 0.5–2% of the volume/hour [4,8]. Under typical conditions, one ton of oil can be physically transported to cover a radius of approximately 50 m with a thickness of 10 mm only ten minutes after the spill occurrence [8]. Oil spills can severely affect the marine environment [9,10], causing changes in the abundance of phytoplankton and other aquatic organisms [11,12], and threatening the coral reefs fringing the Red Sea coast [13]. Timely and accurate detection of oil spills,

and tracking of their spread, are therefore crucial to implement precautionary measures to mitigate their damage [4,14–17]. Traditional oil spill monitoring techniques, including aerial or field campaigns, are demanding in terms of logistics and human resources, and not always efficient at achieving timely and accurate identification of large affected areas. Alternatively, remote sensing methods have become increasingly popular for oil spill detection (e.g., [4,6,8,9,11,13,15–19]).

The synthetic aperture radar (SAR) is an active satellite sensor that has been broadly used for oil spill detection as it provides high-resolution information about an oil spill during day and night, and under all weather conditions [8,14,16,19–24]. SAR detects oil spills through the dampening of the capillary waves generated as a function of wind speed conditions, where oil spills appear darker than the surrounding waters [1]. The surface roughness of the sea with wind speed ranges between 3–6 m/s provides ideal conditions for oil spill detection with SAR [6,8,14,25]. The absence of developed waves during calm wind conditions (i.e., <2 m/s) and high redistribution of the spilled oil during high wind conditions (i.e., >10 m/s), on the other hand, are unfavorable conditions for oil spill detection with SAR [6,19,25]. SAR sensors further suffer from low coverage, long revisit time, and uncertainties in representing natural dark patches caused by various factors, such as wind shadow near islands, high waves, algal blooms, ship wake, and rain cells [4,6,14,21,26]. Optical sensors, which provide a wide swath, daily coverage, and importantly are generally freely available, could complement SAR in detecting and tracking oil spill movement [14,21].

Several studies have investigated the use of multispectral imageries [11,21,22] and optical sensors for oil spill detection [14]. Operational remote sensing sensors, such as Sentinel-2, MODIS, and Landsat-8 have been widely used for monitoring oil spills in several regions around the world [8,15,17,19,27]. Satellite optical sensors acquire data at different ranges of the electromagnetic spectrum, including the visible, near-infrared, shortwave infrared, and thermal infrared regions, which have proven useful for detecting oil spills [4,14,28]. The spectral characteristics of oil spills vary with the oil type and depend on the physical oil characteristics, film thickness, weather, illumination conditions, and the optical properties of the oil and sea [4,11,16,21,22]. An oil spill appears in the visible region of the electromagnetic spectrum (from approximately 400–700 nm) and exhibits relatively higher surface reflectance than the surrounding water. However, it has no unique reflection/absorption features that can directly discriminate oil from the surrounding background [11]. In contrast, the optically-thick oil exhibits different thermal characteristics than the surrounding water [4]. Given that oil absorbs solar radiation and re-emits a portion of this radiation as thermal energy, it exhibits a higher thermal infrared emissivity than water, primarily in the 8–14 μm range depending on the thickness of the oil slick [4,11]. For example, thick oil appears radiometrically hotter in infrared images than the surrounding water during daytime as it absorbs a greater amount of solar radiation. Oil with an intermediate thickness appears cooler; but thin oil or sheens may not be easily detectable [28,29]. The short revisit time and wide coverage of optical satellite sensors compared to SAR make them appealing tools for oil spill detection [19,28,29].

Moderate Resolution Imaging Spectroradiometer (MODIS) optical sensor images have been used to monitor many large oil slicks around the world. For instance, Hu et al. [30] demonstrated MODIS capability for operational oil spill applications in the Gulf of Mexico and the East China Sea. Maiani et al. [22] applied an object-based image analysis (OBIA) on MODIS bands to monitor the Deep Water Horizon oil spill in the Gulf of Mexico. Zhao et al. [31] used different optical satellite missions, such as MODIS, Medium Resolution Imaging Spectrometer Instrument (MERIS), Landsat-7 ETM, and Landsat-8 data to investigate three oil spill events that occurred in the coastal areas of the Arabian Gulf. These studies also suggested that the detection of surface oil slicks with satellite optical images remains challenging because of their sensitive dependence on the physical oil characteristics, sea surface roughness, weather, and illumination conditions [15,28].

This study investigates a multi-mission satellite approach to detect and track an oil spilled into the central Red Sea from a vessel named Sabiti carrying a full load of 1 million barrels of crude oil on 11 October 2019 (RSOS-2019) at 05:00 local time [12,32,33] (Figure 1). The vessel, en-route to Syria via the Suez Canal, started leaking oil approximately 100 km from the Saudi port city of Jeddah (38.33°E , 21.13°N , Figure 1) [8]. The oil patches were observed for up to 17 days after the commencement of the spill. Here, different oil spill detection algorithms are simultaneously implemented to infer the oil locations from Sentinel-1A and 1B SAR images, and optical sensor measurements from Sentinel-2A and 2B, MODIS, Landsat-8, Meteosat, and PlanetScope. To track the time evolution of the oil patches, only Meteosat offers very high temporal (15 min) and spatial coverage of the whole Red Sea to continuously (at an hourly rate) monitor the movement of oil slicks, but at a coarse 1 km resolution. Distinguishing clouds from oil patches with optical images is, however, challenging [14]. We therefore carry out, for the first time, a sequential analysis of Meteosat images to isolate the oil spill regions from clouds based on their brightness and movement. The results suggest that high temporal information may be extracted from a geostationary satellite to detect and track RSOS-2019 in the low-cloud coverage Red Sea region. In addition, we use the high resolution (3 m and daily) PlanetScope images to efficiently track the oil slicks in the coastal areas near Jeddah. The movement of the oil spill is further analyzed based on surface currents from a high-resolution regional reanalysis that has been specifically generated for the Red Sea.

The rest of this study is organized as follows. Section 2 describes the different datasets and algorithms used for oil spill detection. The results of the implemented algorithms for identifying RSOS-2019 are presented in Section 3. The analysis of the oil spill movement in relation to the ocean currents is analyzed in Section 4. A summary of the main findings concludes this work in Section 5.

2. Data and Methods

Sentinel-1 is a constellation of two polar-orbiting satellites (1A and 1B), forming the European Radar Observatory for the Copernicus joint initiative of the European Commission (EC) and the European Space Agency (ESA). It employs a C-band SAR sensor with a central frequency of 5.4 GHz, corresponding to a wavelength of 5.55 cm, and can operate in single polarization (HH or VV) and dual-polarization (HH + HV or VV + VH). Sentinel-1A and 1B acquire microwave images in four exclusive modes: strip map mode (SM), interferometric wide swath (IW), extra-wide swath (EW), and wave mode (WM), providing images with a resolution range of 5–40 m under all weather conditions [18,34]. The two satellites collect data in IW mode and their VV + VH polarization, which allows the combination of a large swath width (250 km) (Table 1). In practice, cross-polarization (i.e., VH and HV) has a much lower intensity and is influenced more by background and instrument noise than the co-polarization (i.e. VV and VH) [8,14,35]. For this reason, SAR data from the VV channel was used [35–37]. The revisit cycle of Sentinel-1A and 1B is 12 days, and approximately six days when combining both [4,14]. Sentinel-1B became not operational since 23 December 2021 (06:53 UTC), reducing the revisit time back to 12 days. A new Sentinel-1C is planned to be launched as soon as by the end of this year 2022.

A total of seven Sentinel-1A and 1B SAR images were available (Table 2) to detect the oil patches during RSOS-2019. The Sentinel-1A and 1B Level 1 IW GRD data was pre-processed with a series of corrections, including orbit file corrections, thermal noise removal, conversion of digital pixel values to radiometrically calibrated SAR backscattering, speckle filtering, terrain corrections, conversion to decibels (dB), etc., as illustrated in Figure 2. Note that continuous scenes in the same track were merged during the pre-processing. The pre-processing step was applied automatically using python programs available from the Sentinel Application Platform (SNAP) Python API provided by ESA. The resolution of the preprocessed SAR results is $20\text{ m} \times 20\text{ m}$, which is similar to the original products. The details of each step-by-step pre-processing methodology, and the description of the main parameters used in the methodology can be found in [35,38] and in Table 3.

Table 1. Characteristics of Sentinel-1 [18].

Parameter	Interferometric Wide Swath Mode (IW)
Swath width	250 km
Incident angle range	29.1–46.0°
Sub-swaths	3
Azimuth steering angle	±0.6°
Azimuth and range look	Single
Polarization	Dual VV + VH
Maximum Noise Equivalent Sigma Zero	−22 dB
Radiometric stability	0.5 dB (3 σ)
Pixel size (meter)	10

Table 2. List of the Sentinel 1 SAR images used in this study.

Satellite	Date	Image
Sentinel 1B	13 October 2019	S1B_IW_GRDH_1SDV_018451_022C28_AA13
Sentinel 1B	13 October 2019	S1B_IW_GRDH_1SDV_018451_022C28_9E30
Sentinel 1A	14 October 2019	S1A_IW_GRDH_1SDV_029449_03598E_1B6C
Sentinel 1B	22 October 2019	S1B_IW_GRDH_1SDV_018590_023066_0FFE
Sentinel 1B	22 October 2019	S1B_IW_GRDH_1SDV_018590_023066_ECE4
Sentinel 1B	25 October 2019	S1B_IW_GRDH_1SDV_018626_023181_36B9
Sentinel 1A	26 October 2019	S1A_IW_GRDH_1SDV_029624_035F8D_0944

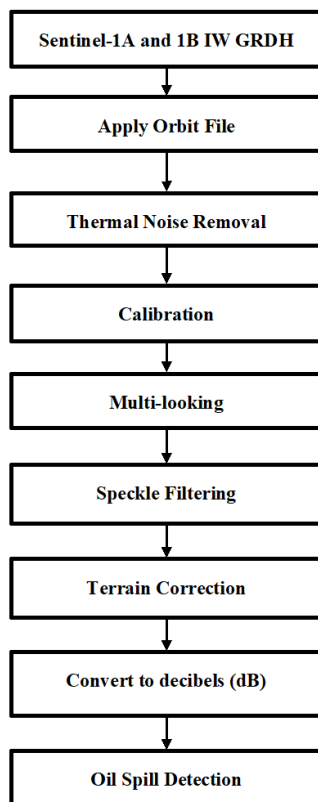
**Figure 2.** Sentinel-1 GRD pre-processing workflow.

Table 3. List of the main parameters used in SNAP pre-processor module to process Sentinel-1 SAR images.

Operator	Parameter	Value
Read	Data format	Any format
Apply orbit file	Orbit state vectors Polynomial degree	Sentinel precise 3
Calibration	Polarizations Output sigma0 band	VH, VV True
Terrain correction	Source bands band DEM DEM resampling method Image resampling method Pixel spacing	Sigma0_VH, Sigma0_VV SRTM 1Sec HGT (Auto Download) Bilinear interpolation Bilinear interpolation 10 m
Speckle filtering	Source band Filter	VV Refined Lee
Convert to dB	Source bands	VV
Write	Save as	GeoTIFF—BigTIFF

The water surface roughness is a key factor for detecting oil spill with SAR [35,37]. Wind-induced friction between the air and water surface generates gravity capillary waves in the range of millimeters to centimeters [8,14,23,35]. Oil slicks can dampen capillary waves and short gravity waves, and thereby reduce the sea surface roughness. This reduces the magnitude of radar backscattering over oil-covered waters compared to the surrounding area, with the sea surface appearing as dark patches in SAR images [35,37].

The identification of oil slicks from SAR images depend on the weather conditions, especially wind speed [8,14,35,37]. In general, suitable ranges of wind speeds for oil slick detection by SAR are 1.5 to 10 m/s [14,35–37]. At high wind speeds (>10 m/s), waves can break up oil into smaller droplets, which may prevent an effective detection of oil slicks [35–37]. The oil detection with SAR also becomes more challenging at lower wind speeds (<1.5 m/s), since calm sea conditions can be also seen as dark patches by SAR. “Look-alike” features in SAR could also be caused by other natural phenomena, such as natural films, wavefronts, wind sheltering by land, rain cells, internal waves, upwelling, and eddies [14,35,39–41]. Distinguishing oil spills from look-alikes is a challenging task for oil spill detection with SAR [14,35,37]. Here, we discriminated oil slicks based on: (i) the referred range (−18 to −35 dB) of radar backscatter values [26,37,42], (ii) the temporal changes in positions and shape of the oil [36,37], and (iii) the texture of the dark features [8,14,35–37]. After determining the positions of the oil slicks, we further examined the delineated oil slick through visual checks [35,37,43].

Multi-Spectral Instrument (MSI) spectral band images of Sentinel-2A and 2B, with a swath width of 290 km and ten day revisit time at the equator, are also available to detect the RSOS-2019. Sentinel-2A and 2B operate four visible, and one near-infrared, bands at 10 m resolution, six red-edge shortwave infrared bands at 20 m resolution, and three atmospheric correction bands at 60 m resolution. The Sentinel-2A and 2B Level-1C data were converted to level-2A products by applying atmospheric corrections with the commonly used ACOLITE processor [44]. ACOLITE was specifically developed for marine, coastal, and inland waters by the Royal Belgian Institute of Natural Sciences (RBINS) and supports the processing of Sentinel-2 images [44]. ACOLITE outputs reflectance in all visible and NIR bands, sampled on a 10 m pixel grid for Sentinel-2. After that, to map the oil, the Oil Spill Index (OSI) is implemented as described in Equation (1) using Sentinel-2A and 2B visible bands (*BO4*, *BO3*, and *BO2*) [21,40].

$$\text{OSI} = \frac{(BO3 + BO4)}{BO2} \quad (1)$$

Bands BO_3 and BO_4 represent the shoulders, and BO_2 represents the nearest band to the absorption features.

We also processed Landsat-8 Level 1 (L1T) data from the Operational Land Imager (OLI) and Thermal Infrared Sensor (TIRS) bands (Table 4). OLI is a push-broom sensor that collects data in the visible, near-infrared, short wave infrared wavelengths, and a panchromatic band [14]. It also operates a further two new spectral bands: a deep-blue band for coastal water and aerosol studies (band 1), and a band for cirrus cloud detection (band 9). TIRS collects data in two long-wavelength thermal infrared bands at 100 m spatial resolution. Landsat-8 images cover an area of 185 km \times 185 km with a revisit cycle of 16 days. The Landsat-8 RGB (Red (R), Green (G), Blue (B)) images are generated by filtering the OLI bands 4, 3, and 2. We also estimated the brightness temperature using a digital number (DN) from Landsat-8 thermal band 10 metadata. The algorithm for estimating brightness temperature involves two steps [14]:

Table 4. List of satellite data used in this study.

Satellite	Spectral Region (Bands)	Range (μm)	Spatial Resolution	Revisit Time	Operation	Level
MODIS (Aqua)	VIS, NIR, MIR, SWIR, LWIR (36 bands)	B1-19 (0.405–2.155), B20-36 (3.66–14.28)	250, 500, 1000 m	1–2 day	2002	L1B
Landsat-8	VIS, NIR, SWIR, TIR (12 bands)	B1-9 (0.43–1.38), B10-11 (10.6–12.51)	15, 30, 100 m	16 day	2013	L1T
Meteosat	VIS, NIR, IR, HRV	B1-3 (0.6–1.7) B4-11 (3.8–14) B12 (0.5–0.9)	3 km, 1000 m	15 min	2002	Level 1.5
PlanetScope	VIS, NIR (4 bands)	B1 (0.45–0.51) B2 (0.50–0.59) B3 (0.59–0.67) B4 (0.73–0.74) B5 (0.78–0.86)	3 m	Daily	2016	PS2
Sentinel-2	VIS, NIR, SWIR (12 bands)	0.443–2.190	10, 20, 60 m	5 day	2015	L1C

(a) The Landsat 8 Level 1 (L1T) band 10 values are first converted into top of atmosphere (TOA) radiance using the following equation [14]:

$$L_\lambda = M_L Q_{cal} + A_L \quad (2)$$

where L_λ denotes the spectral radiance, M_L (=0.000334) the band-specific multiplicative rescaling factor, A_L (=0.10000) the band-specific additive rescaling factor, and Q_{cal} the quantified and calibrated standard product pixel values.

(b) Calculation of brightness temperature (BT) using the DN values as:

$$BT = \frac{K_2}{\ln\left(\frac{K_1}{L_\lambda + 1}\right)} \quad (3)$$

where BT denotes the brightness temperature, and K_1 (=774.8853) and K_2 (=1321.0789) are the thermal conversion constants.

MODIS operates on Terra and Aqua spacecraft viewing swath width of 2330 km every one to two days. It measures the radiance at the TOA in 36 spectral bands varying between 0.405 μm and 14.385 μm (Table 4). The fluorescence/emissivity index (FEI) was computed

to account for the higher reflectance of oil in the blue wavelength (induced by reflected light) and lower emissivity in the thermal infrared region using [11,22]:

$$FEI = \frac{\rho_{Blue} - \varepsilon_{Thermal}}{\rho_{Blue} + \varepsilon_{Thermal}} \quad (4)$$

where ρ_{Blue} denotes the reflectance calculated from the MODIS spectral band 3 (0.459–0.479 μm), and $\varepsilon_{Thermal}$ denotes the emissivity calculated from the MODIS spectral band 31 (10.780–11.28 μm).

We further analyzed the Meteosat Second Generation (MSG) satellite hourly data available during daytime to track the RSOS-2019 oil patches. MSG is a geostationary satellite providing continuous surface and atmospheric information every 15 min, but at a coarse resolution of 1 km. The onboard Spinning Enhanced Visible and Infrared Imager (SEVIRI) instrument measures the spectral and emitted radiances in 12 channels with wavelengths of 0.6–1.6 μm for visible/near-infrared channels and 3.8–14 μm for infrared channels. We processed the MSG High-Resolution Visible channel (HRV) Level 1.5 images to identify the intensity of the RSOS-2019 on the sea surface.

We further acquired the PlanetScope RGB (bands 4, 3, and 2) composite images to track the spread of RSOS-2019 near the coast. PlanetScope is a commercial constellation composed of approximately 175 satellites, enabling full scanning of the entire earth land/water surface within a day (<https://www.planet.com/products/planet-imagery/> (accessed on 19 February 2021)). It provides four spectral bands (Blue, Green, Red, and Near-Infrared), represented by visible and near-infrared (VNIR) with a spatial resolution of 3 m. We used the pre-processed RGB composite images from 12 October 2019, to 17 October 2019 (except for 14 October 2019, for which an image was not available) and Sentinel Application Platform (SNAP) 5.0 software to pre-process the images.

To analyze the oil spill movement in relation to the prevailing ocean currents, we analyzed the ocean velocity fields from a high-resolution regional ocean reanalysis specifically produced for the Red Sea at 4 km resolution [45]. This new reanalysis has been generated using an Massachusetts Institute of Technology general circulation model (MITgcm) and a hybrid ensemble data assimilation system incorporating available in-situ temperature and salinity profiles, and remotely-sensed satellite sea surface temperature and sea surface height observations [45,46]. The MITgcm domain (30°E–50°E and 10°N–30°N) covers the entire Red Sea, including the Gulf of Suez, the Gulf of Aqaba, and part of the Gulf of Aden connected to the Arabian Sea. The model was implemented on a spherical polar grid at an eddy-resolving horizontal resolution of $0.04^\circ \times 0.04^\circ$ and 50 vertical layers, with 4 m spacing on the surface and 300 m spacing near the bottom. Full details of the model, assimilation scheme, and the resulting reanalysis can be found in [45,47,48].

3. Remote Sensing RSOS-2019

The RSOS-2019 spread was detected using all available satellite imageries described in Section 2. Specific algorithms were implemented for each imagery and inferred oil slicks were segmented accordingly. SAR and optical sensors follow different mechanisms to detect oil spills and the analysis presented here allowed us to examine the capability of each imagery and their relevance for operational monitoring in the context of RSOS-2019.

The spread and propagation of RSOS-2019 was first inferred from the Sentinel-1A and 1B SAR images available on (i) 13 and 14 October 2019 (two days after the spill), (ii) 22 October 2019 (12 days after the spill), (iii) 25 October 2019 (15 days after the spill). The images of the radar backscatter, due to the dampening of the short surface waves, clearly indicate dark patches over the accident area between 13 and 14 October (Figure 3a). Two days after the accident, the SAR images showed oil slicks following a circular pattern with dark patches elongated both north and south of the incident location. The dark red line indicates the outline of the oil slick (Figure 3b). The circular pattern area was observed in the VV mode, and the movement of oil largely expanded to the south of the incident location (Figure 3a,b) under the action of winds and ocean currents [4]. No oil patches

were observed at the incident location in the SAR images twelve days after the accident (Figure 3c–f). After twelve days, the spilled oil moved eastward towards the coastal region near Jeddah port.

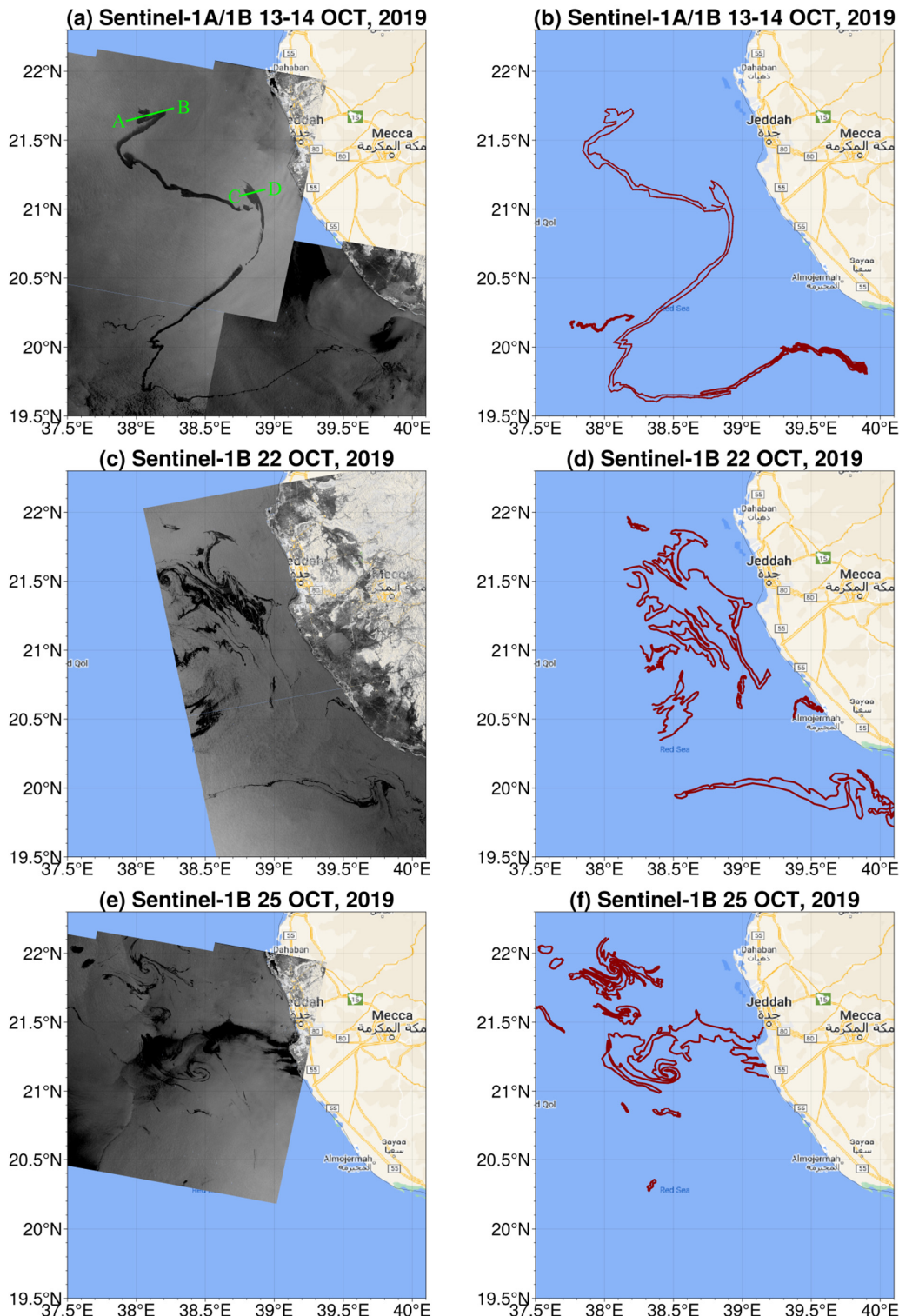


Figure 3. Mosaic of Sentinel-1A and Sentinel-1B imageries collected on (a) 13 and 14 October 2019 (two days after the spill), (c) 22 October 2019 (12 days after the spill), (e) 25 October 2019 (15 days after the spill). Panels (b,d,f) are the same as (a,c,e), except that they use a dark red line to indicate the outline of the oil spill.

To examine changes in the intensity of the radar backscattering over the oil patches and surrounding waters, we analyzed the radar backscattering intensity values (Figure 4a,b) at two cross-sections AB and CD, as indicated in Figure 3a. The intensity values from A to B and C to D show that pixels can be associated with low and high values, clearly distinguishing the oil spill from the surrounding water, respectively. Although SAR oil detection algorithms are widely considered to be the most efficient at demarcating oil slicks [8,14,19,23], their relatively long revisit time (~12 days) limits their potential for operational purposes, which clearly demands higher temporal resolution images.

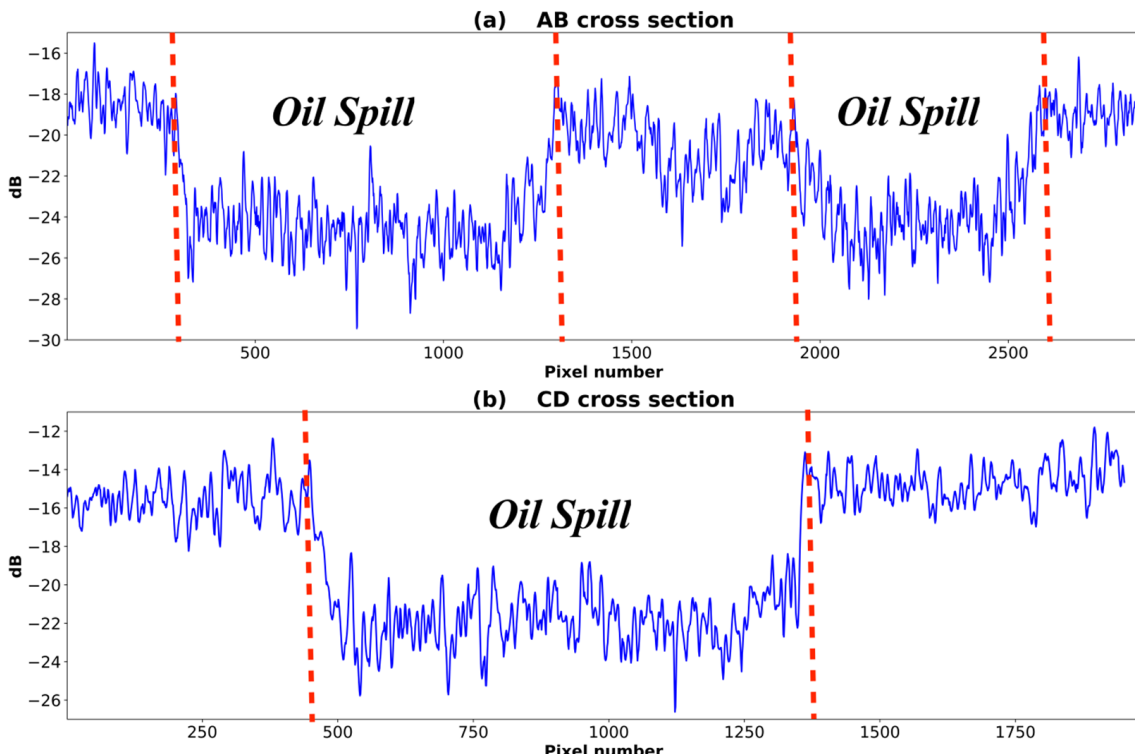


Figure 4. The intensity of the radar backscattering (Y-axis) at each pixel (X-axis) along the cross-sections (a) AB and (b) CD (shown in Figure 3a) from Sentinel-1 SAR images on 13 October 2019 (two days after the spill). The pixel numbers with low/high intensity values are associated with oil/water.

We then investigated the oil slick propagation by processing the optical satellite images. The OSI was first computed to characterize the oil spill using different spectral bands from the Sentinel-2A and 2B MSI images available on 12, 17, and 27 October 2019 (i.e., 1 day, 7 days, and 17 days after the spill) [25,29]. The OSI image on 12 October shown in Figure 5a indicates the oil spill as a dark narrow line; the clouds over the region appear in red, and the outline of the oil spill in dark red (Figure 5b). Seven days after the spill (17 October), the OSI images show a wide spread of the oil (Figure 5c,d). The images on 27 October (Figure 5e,f) suggest a reduction in the oil coverage. The Sentinel-2A and 2B OSI images clearly demarcated the distribution of the oil spill and its spread, in good agreement with those of SAR.

We further computed the FEI from the MODIS L1B Aqua satellite images on 11 and 13 October. The image on 12 October (one day after the spill) could not be used due to significant cloud coverage over the spill region. The resulting FEI maps (Figure 6) exhibit higher brightness in the oil-affected areas compared to the adjacent oil-free areas. The FEI images on the accident day (11 October) indicate a narrow patch with slightly reduced brightness compared to the adjacent water (Figure 6a), in agreement with Sentinel-2 images, suggesting that the ship sailed southward while leaking oil. More oil patches of low brightness were captured by MODIS at the southeast corner of the narrow slick. Two days after the accident (13 October), these oil patches spread northward and eastward towards

the coastal regions, reaching a few tens of kilometers away from the Jeddah port, as shown by the MODIS images (red line; Figure 6b). The MODIS FEI and Sentinel-1 SAR inferred oil spills on 13 October are in agreement, except for the northward patches detected by MODIS as further analyzed and discussed below.

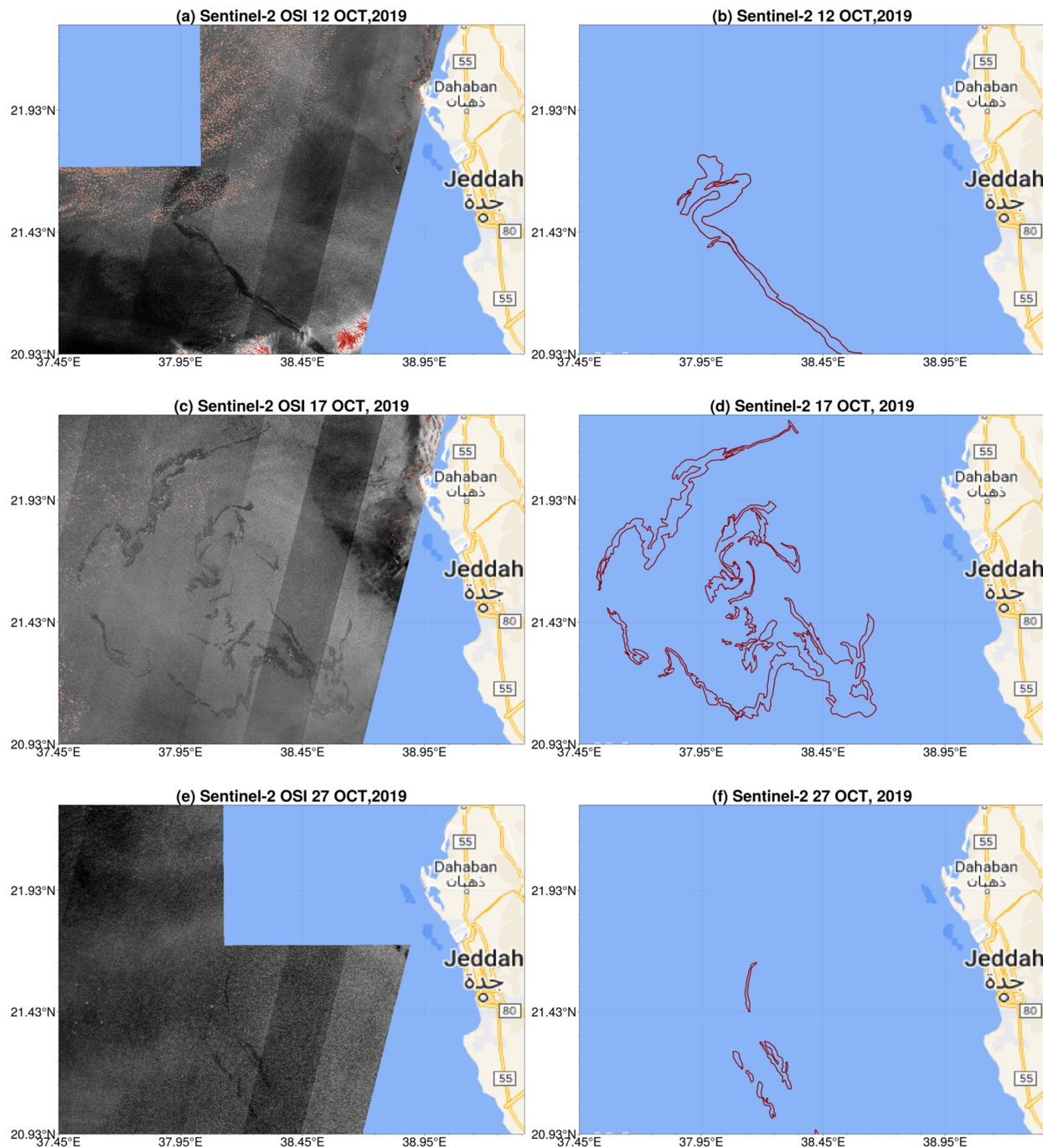


Figure 5. The Oil Spill Index (OSI) values of Sentinel-2 images on (a) 12 October 2019 (one day after the spill), (c) 17 October 2019 (7 days after the spill), (d) 27 October 2019 (17 days after the spill). Panels (b,d,f) are same as (a,c,e) except that they use a dark red line to indicate the outline of the oil spill.

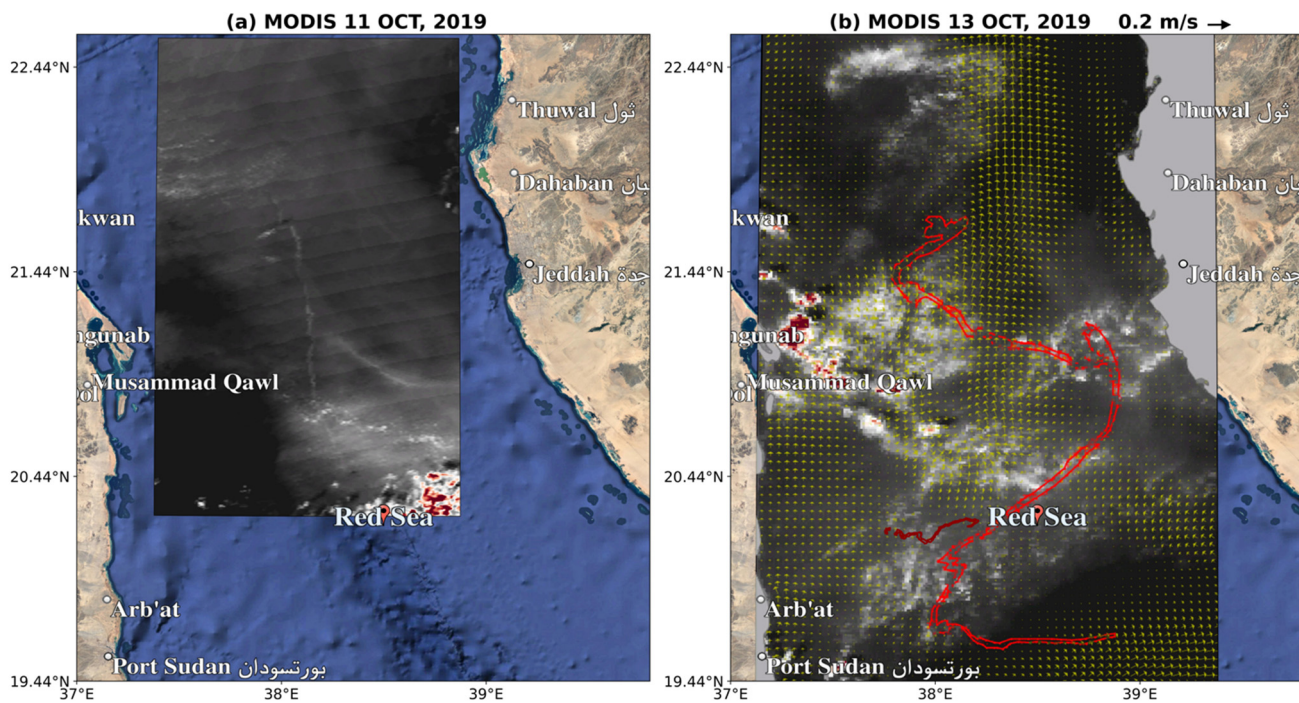


Figure 6. MODIS FEI images on (a) 11 October 2019 (the day of the accident); (b) the vectors overlaid on the MODIS image of 13 October 2019 (two days after the accident) are the model surface currents corresponding to the same day. The red line indicates the outline of the oil slick from Sentinel-1 SAR at 03:30 UTC on 13 October 2019.

Only one Landsat-8 L1T image was available during the RSOS-2019 on 13 October, with a high spatial resolution (approximately 15–100 m) but narrow coverage (185 km). The spectral radiance of this image was converted to brightness temperature using the thermal band 10. A Red-Green-Blue (RGB) composite image was also generated using visible spectral bands to identify the oil spill. The Landsat-8 RGB composite image clearly distinguished the contrast between oil and water, detecting oil patches in agreement with the corresponding SAR (Figure 7). Figure 8 displays the BT from 299 K–300 K, where the oil-affected areas can be detected as patches with different contrast to the non-affected surrounding area, also in agreement with those detected by SAR. High/low BT values (more/less than 300.25 K) indicate the affected/non-affected oil spill areas. Oil absorbs heat in the daytime, becoming warmer than the surrounding water, so that oil slicks are visible as hot patches on the thermal image (Figure 8). Klemas [49] classified the thermal response to oil thickness, where thicker oil appears hotter or brighter than thin oil. Here, the thick oil spill regions also show higher BT values than the surrounding thin oil areas. Overall, the oil detected in the coastal areas by Landsat-8 images agree well with the Sentinel and MODIS FEI images (Figure 6b).

The hourly MSG satellite HRV channel images did not show distinct features related to the oil spill on 11 October (figure not shown), while the MODIS FEI image indicated a narrow patch with a less bright color region than the surrounding area (Figure 6a) on the same day at 10:00 UTC. This could be due to the low number of spectral bands and the coarse resolution of MSG images. MSG images were not processed on 12 October because of significant cloud coverage over the incident area. On 13 October, the MSG images at 10:00–10:30 UTC indicated bright circular oil patterns south of the incident location (Figure 9a,b). The clouds in these images exhibited higher brightness (red color) than the oil spill areas. One hour later (11:00 UTC), the clouds moved towards the northern and northwestern parts of the Red Sea, and the spilled oil became more visible (Figure 9c). The clouds then moved towards the west coast and a circular pattern of spilled oil, elongated in the north-south direction, appeared (Figure 9d). This allowed us to distinguish the clouds

from the oil patches in this sequence of images based on cloud brightness and movement, because the clouds moved faster and exhibited higher brightness than the oil patches.

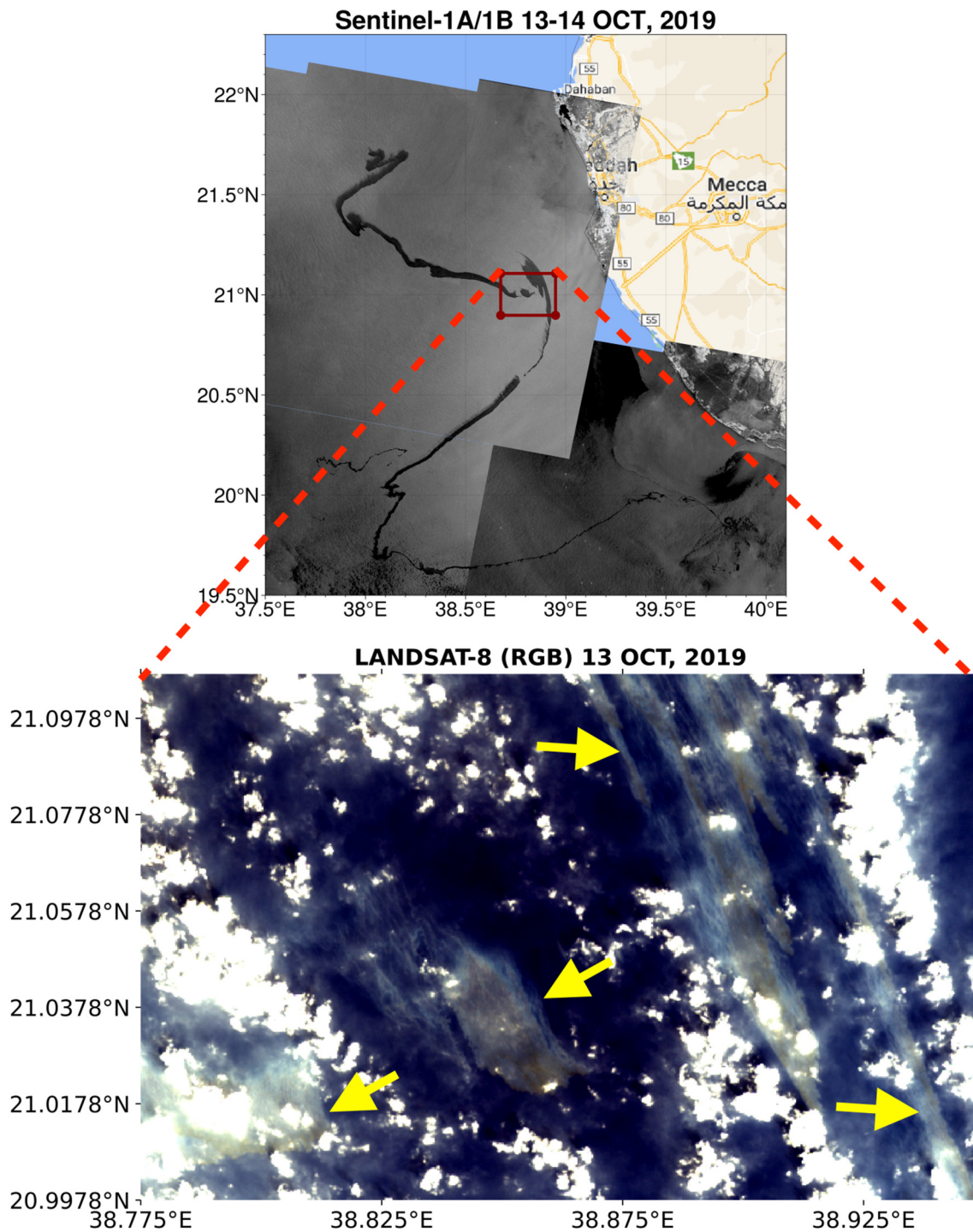


Figure 7. The oil spill using Sentinel-1 imagery on 13 October 2019. The oil-spill using the Lansat-8 OLI visible bands (RGB) composite image was available for the zoomed region of the Sentinel-1 imagery on 13 October 2019. The yellow arrows indicate the oil slicks.

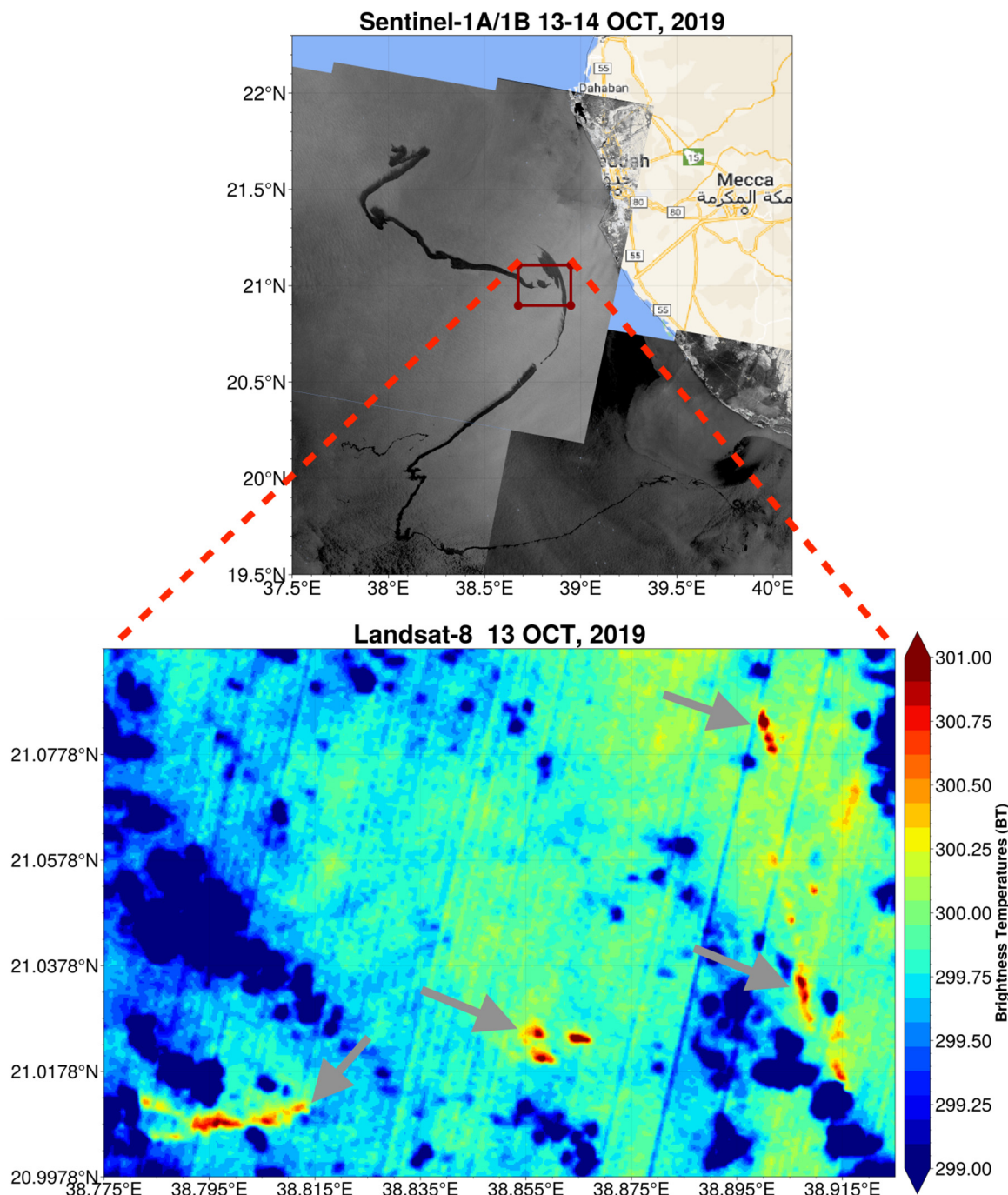


Figure 8. Same as Figure 7, but for the brightness temperature for Lansat-8 thermal band 10 on 13 October 2019. The gray arrows indicate the oil slicks.

The inferred movement of oil by MSG accords with the surface currents that depicted a mesoscale eddy in the middle of the basin, connecting the southeastward flow to strong northward-flowing currents in the east (Figure 10a–d). The oil patches were not detectable in the MSG images after 13 October because of the weaker brightness of the diluted oil patches in the subsequent days and the limited number of spectral bands of MSG. The widespread oil patch movements towards the north and Jeddah featured in MODIS (Figure 6b), Landsat-8, and MSG, were detected as a narrow oil slick in Sentinel-1 SAR despite reasonable spatial coverage. This could be due to the difficulties of SAR to detect oil slicks during the high wind conditions that prevailed over the region (figure not shown), which resulted in mixing of oil and water [36,42].

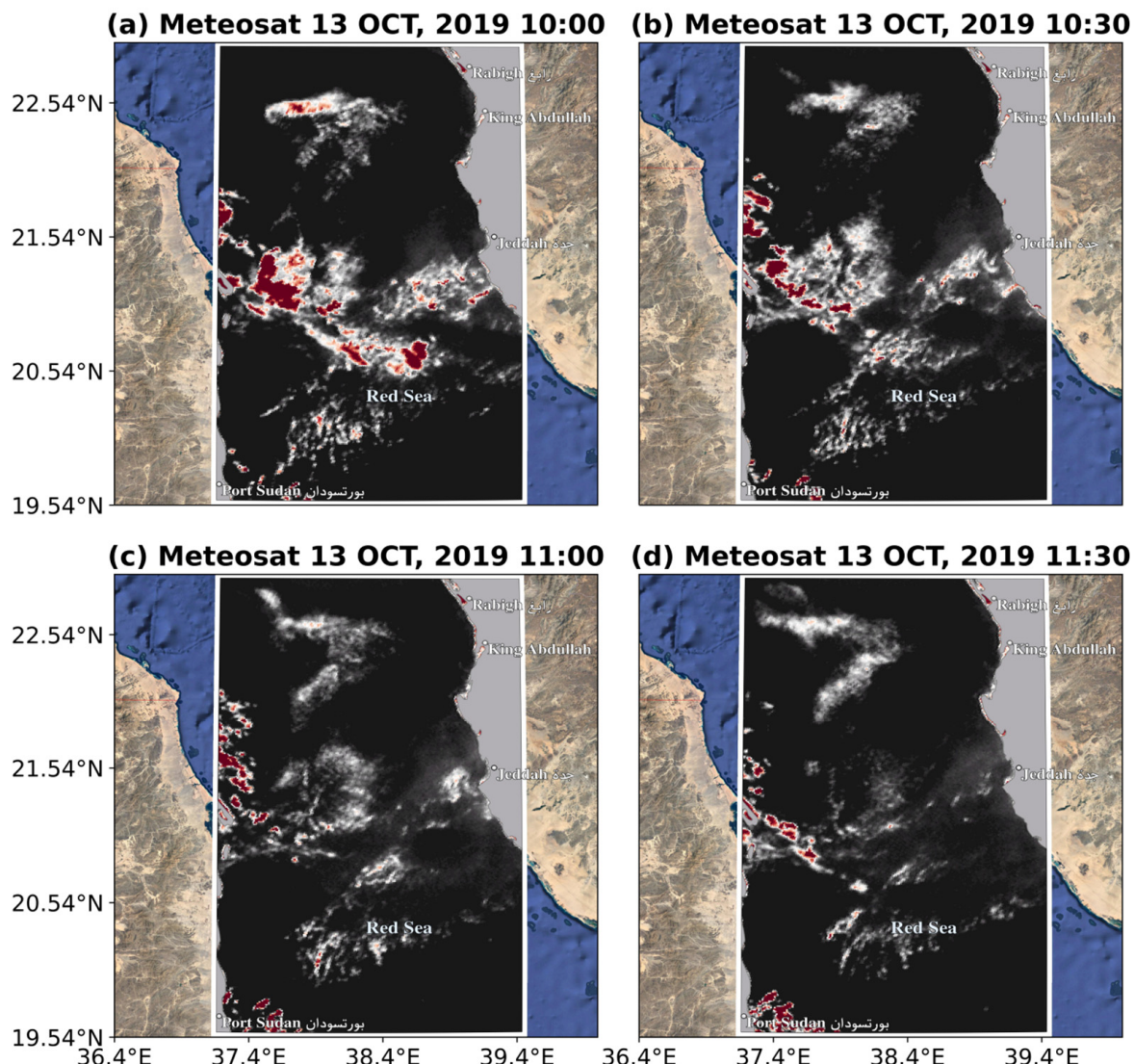


Figure 9. Meteosat HRV channel Level 1.5 images at 10:00 UTC, 10:30 UTC, 11:00 UTC, and 11:30 UTC on 13 October 2019.

To follow the oil slick movements near the coastal regions, we processed the RGB (bands 3, 2, and 1) composite of the high-resolution PlanetScope images, which provide daily 3 m spatial resolution images but only cover a distance of 20–25 km from the coast. PlanetScope images revealed no presence of oil on 12 and 13 October (one and two days after the spill, respectively) on the Saudi coast (Figure 11a,b), in line with Sentinel-1 SAR images which revealed the oil slicks at a distance of approximately 30 km from the coast (Figure 3a) on 13 October. PlanetScope images were not available on 14 October, but Sentinel-2B provided a 10 m resolution image that indicated a thin line of oil slicks 12 km from the Saudi coast (Figure 11c). A PlanetScope image on 15 October (four days after the spill) showed oil slicks 7 km from the coastal areas (Figure 11d), which moved to approximately 2 km from the coast on 16 October (Figure 11e), before beaching on 17 October (Figure 11f).

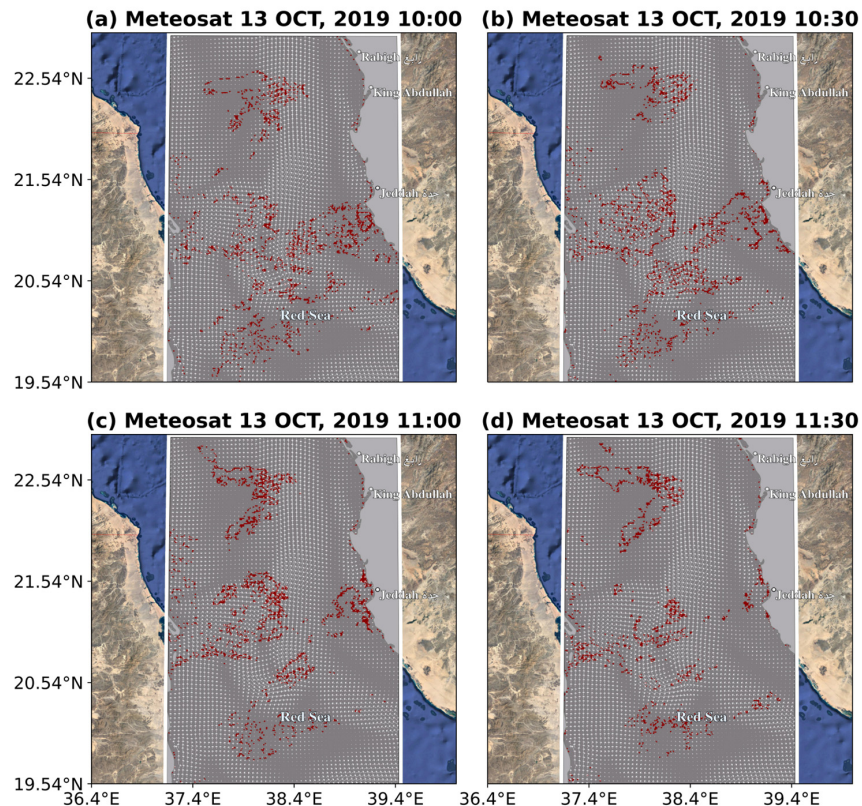


Figure 10. Snapshots of Meteosat detected oil contours, after removing clouds, overlaid on model surface currents at (a) 10:00, (b) 10:30, (c) 11:00, and (d) 11:30 UTC on 13 October 2019.

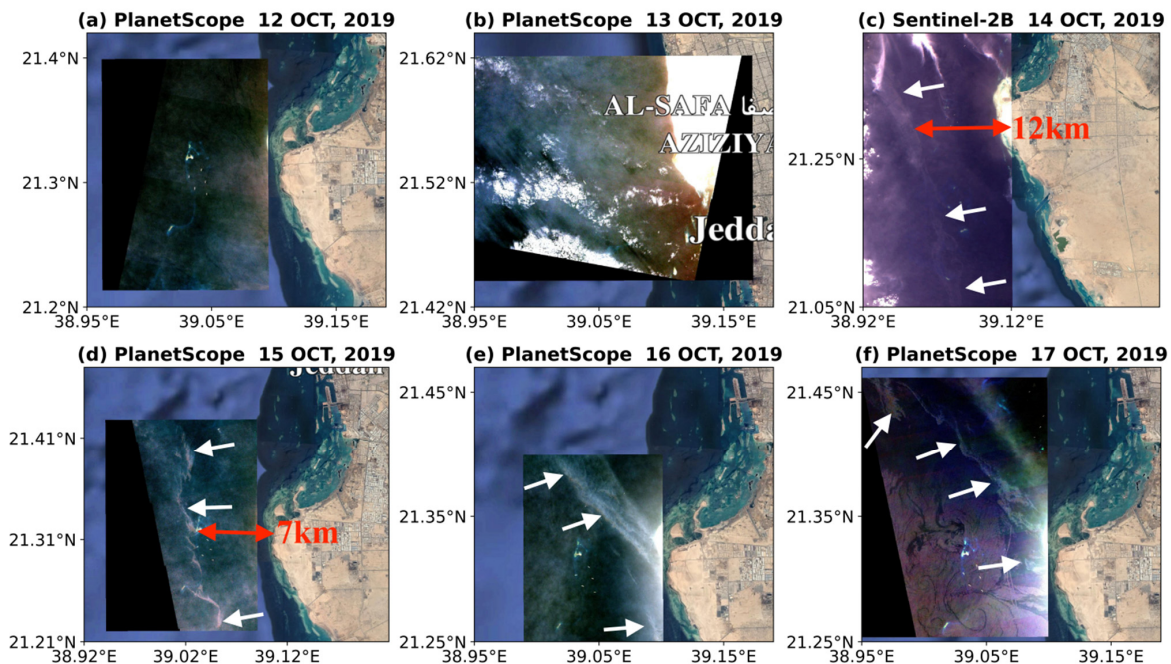


Figure 11. PlanetScope images on (a) 12 October 2019 (one day after the spill), (b) 13 October 2019 (two days after the spill), (d) 15 October 2019 (four days after the spill), (e) 16 October 2019 (five days after the spill), (f) 17 October 2019 (six days after the spill), and (c) the Sentinel-2A RGB (432) color composite image on 14 October 2019 (three days after the spill). The oil slicks detected from the images and their distances from the coast are labeled on the images. The red double arrows represent the distance of the oil spill from the coast and the white arrows indicate the oil slicks.

4. Analysis of the Inferred Oil Spill Movement in Relation to Ocean Currents

Earlier studies have suggested that ocean currents are the predominant drivers of oil spreading, followed by winds [50,51]. We have examined the wind conditions over the oil spill region and found that they were predominantly calm during the Sabiti oil spill event (figure not shown), a climatological feature of this region during this time of the year [52–54].

Figures 12 and 13 outline the spread and movement of the RSOS-2019 oil spill as inferred by the different satellite sensors. The contours on the map indicate the detected oil patches and the vectors in the background depict the prevailing surface currents. A narrow oil slick ~120 km in length and oriented in the north-south direction appeared on 11 October (the day of the accident) in the MODIS image (Figure 12a). The trajectory of the initial oil spill bisected a mesoscale cyclonic eddy (CE) between 20°N and 21.75°N, a feature associated with the meandering of the thermohaline induced boundary current when it veers from west to east [55–59]. The strong speed of the CE moved the spilled oil in the northeast and eastward directions, as indicated by the Sentinel-2 images on 12 October (Figure 12b). The optical satellite images provided limited information about the spill on 12 October, due to widespread cloud coverage over the central Red Sea. The multi-satellite images on 13 and 14 October indicated that the tanker continued to leak oil as it traveled at least as far as 19.5°N. For instance, sentinel-1 SAR images show a narrow oil slick spanning latitudes 19.5°N–21.75°N (Figure 12c). The contours of the detected oil meandered about CE in the north before the oil trajectory became flat in the south at 19.6°N latitude, where a strong eastward current prevailed. The meandering trajectory of the oil in the north and the flat trajectory in the south may be associated with strong advection by ocean currents associated with the dipole eddy centered around 19°N (CE in the north and an anti-cyclonic eddy in the south), an extended feature generated by the seasonal cross-basin wind jets emanated from the Tokar gap during July–August [60,61]. MODIS and MSG images on 13 October also showed the advected and dispersed oil as scattered patches rather than a continuous line (Figures 6b and 9). These patches were advected further east by 14 October, as shown by Sentinel-2 (Figure 12c). Some of these oil patches abutted the Jeddah coast in the subsequent days, as revealed by the 3m resolution PlanetScope images (Figure 11). The remaining patches in the open ocean near the CE of the dipole eddy moved northward by 17 October under the influence of a northward flow (Figures 12d and 13a). Later, after the weakening of the dipole eddy's CE, thermohaline induced northward flowing eastern boundary currents prevailed in the central Red Sea [55–58], ultimately moving the oil patches close to the Jeddah coast after 22 October (Figure 13b,c). The oil patches practically disappeared from the incident site by 27 October (Figure 13d).

The combination of the different satellite missions provided robust information about the oil spill and the progression of its spread, allowing us to fill the spatial and temporal gaps in the individual images (Figure 14) to enable effective monitoring of the oil spill movement of RSOS-2019.

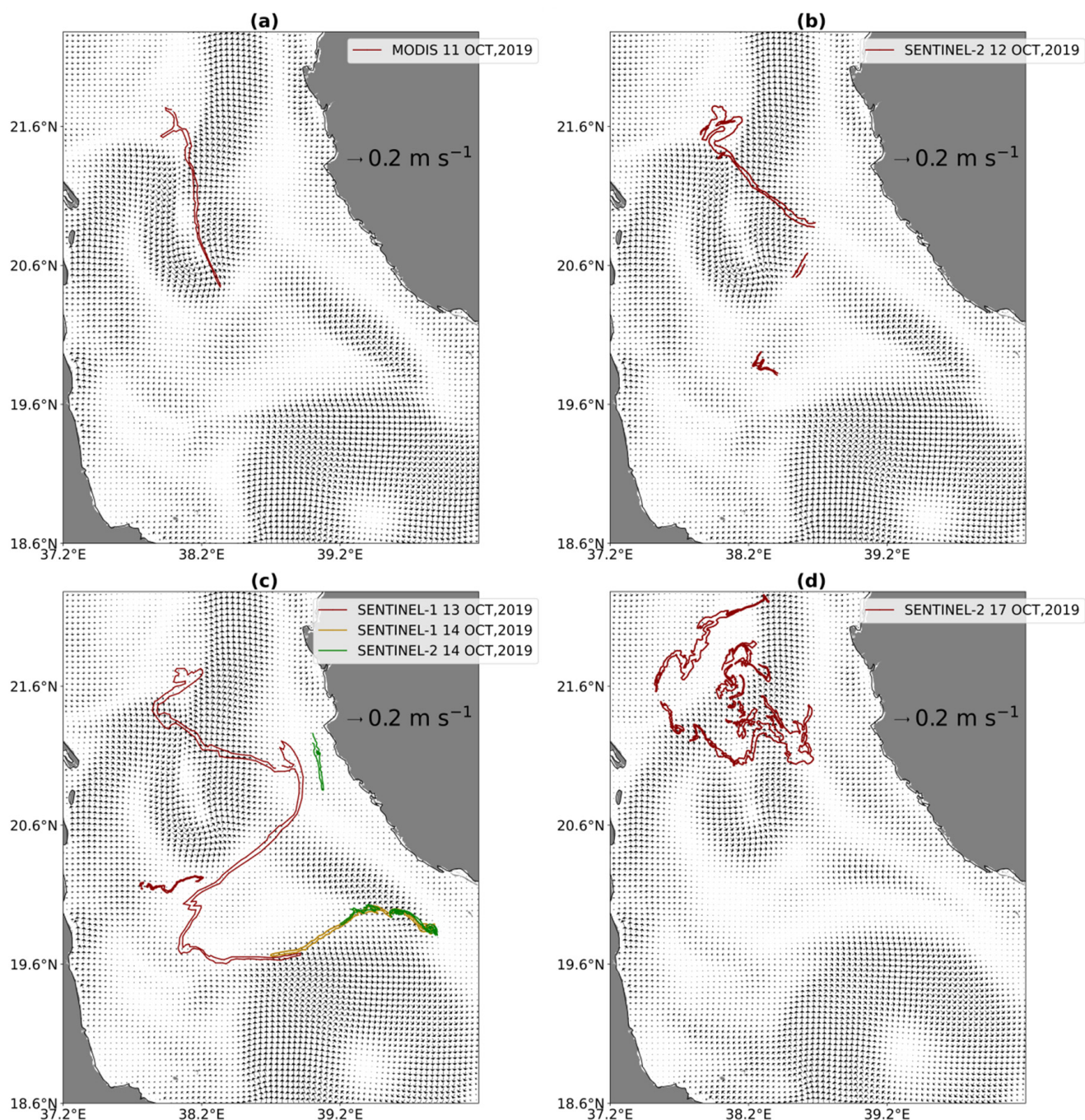


Figure 12. Evolution of model surface currents against the different satellite observations corresponding to (a) 11 October 2019 (the day of the accident), (b) 12 October 2019 (one day after the spill), (c) 13 and 14 October 2019 (two days after the spill), (d) 17 October 2019 (seven days after the spill). Color contours indicate the extent of the oil spill from different satellite observations.

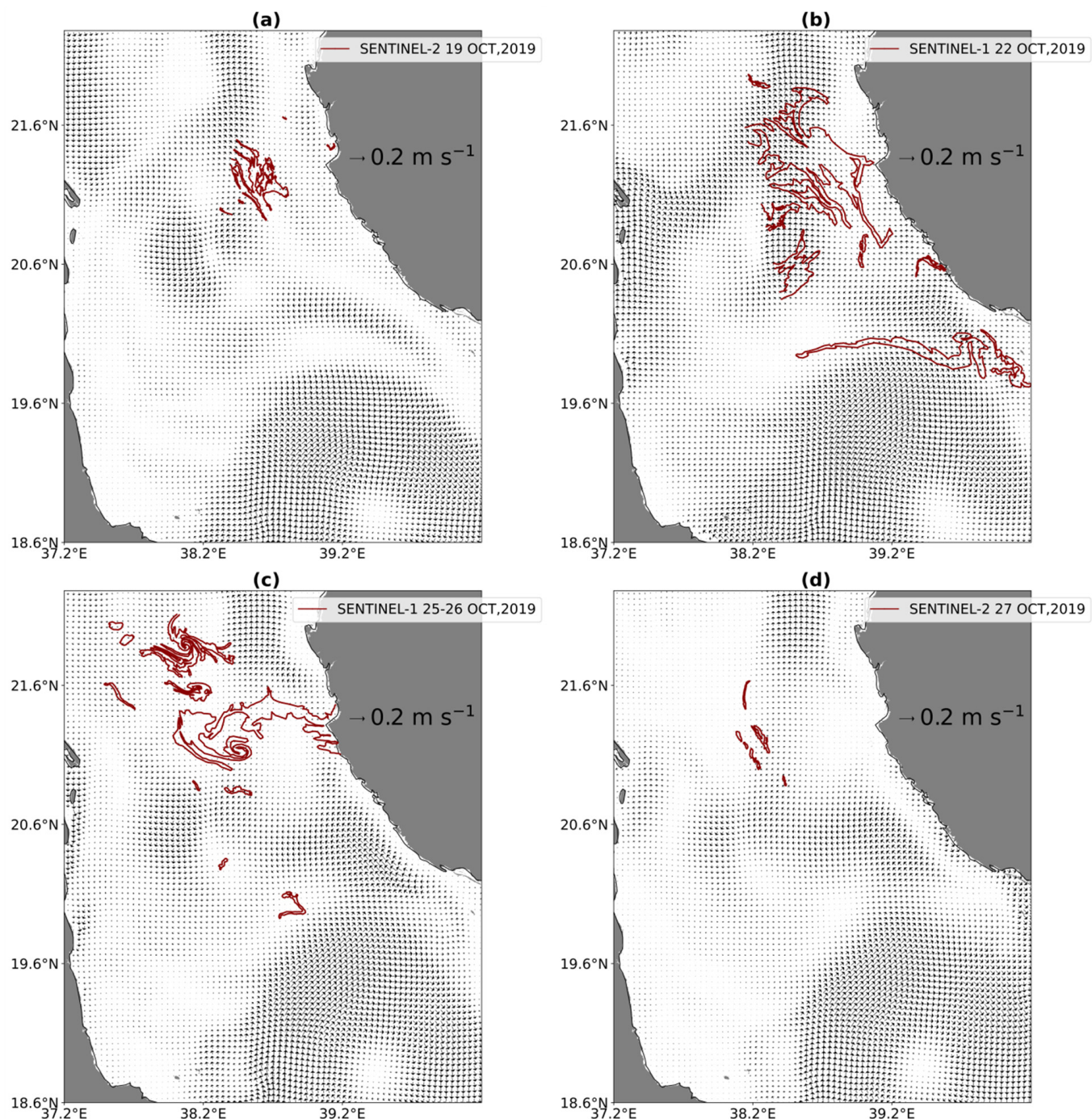


Figure 13. Same as Figure 12, but for (a) 19 October 2019 (nine days after the spill), (b) 22 October 2019 (twelve days after the spill), (c) 25 and 26 October 2019 (fifteen days after the spill), and (d) 27 October 2019 (seventeen days after the spill).

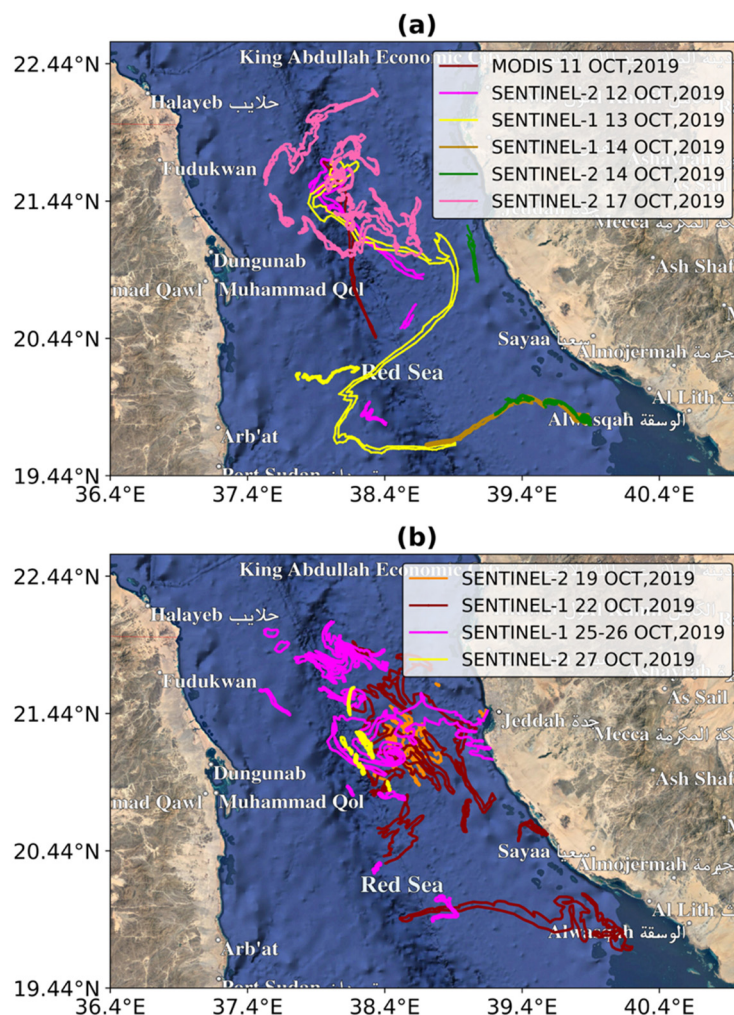


Figure 14. Spread and progression of the oil spill from the Sabti oil tanker as inferred from the different satellite imageries shown in (a) from 11 to 17 October 2019 and (b) from 19 to 27 October 2019. The different colored lines indicate the extent of the oil spill on the different days.

5. Summary and Conclusions

We investigated multi-mission satellite imageries to detect and track an oil spill event that occurred in the central Red Sea on 11 October 2019, following an alleged attack on the Iranian tanker Sabti. Satellite images from Polar-orbit Sentinel-1 SAR, Sentinel-2, MODIS, Landsat-8, PlanetScope satellites, and the geostationary Meteosat were collected and processed before, during, and after the incident. Dedicated oil spill detection algorithms were implemented for each satellite imagery to identify the oil location and its movement. In addition, high resolution surface currents were analyzed to better understand and track the oil spill movement. The satellite images showed that the oil patches remained on the ocean surface for at least 17 days, favored by lower evaporation rates due to calm wind conditions. Therefore, the prevailing surface ocean currents predominantly explained the propagation and spreading of the oil.

The main results of this study can be summarized as follows:

Sentinel-1A and 1B SAR images efficiently detected the oil slicks and indicated north-south and eastward oil patch movements. However, the long (approximately 12 days) revisit time limits their potential for operational purposes.

The oil spill index (OSI) computed using the Sentinel-2A and 2B band ratios identified the dark patches of the oil spill and their spread from the date of the incident up to three weeks afterwards. The oil patches detected by the Sentinel-2A and 2B images agreed well

with the SAR images, but suggested a wider spread due to the advantage of Sentinel-2 in detecting oil patches well mixed with water.

The FEI algorithm implemented to detect oil spills from the MODIS L1B aqua satellite imagery indicated a narrow patch of oil on the day of the accident (11 October 2019), which suggested that the ship continued to leak oil while sailing. Widely dispersed oil was observed towards the east coast of the Red Sea (approximately 30 km away from Jeddah Port) two days after the accident (13 October 2019), in agreement with SAR images.

The only available Landsat-8 RGB composite image during the spill clearly detected the oil spill patches. The brightness temperature (BT) analysis of the image indicated high BT values of more than 300.25 K over the oil locations and smaller values of less than 300.25 K over the non-affected areas.

A sequence of images from the coarse resolution MSG on 13 October detected widespread oil patches and their movements. These patches were identified after distinguishing them from the overlying clouds based on the differences in their movements, directions, and displacement rates. On that day, the oil moved slowly in the eastward direction while the clouds moved faster towards the west.

PlanetScope high-resolution images were highly useful for identifying the oil slicks and their movement over the coastal areas. These indicated that the spilled oil moved about 5 km towards the coastal regions between 14–17 October and beached on 17 October.

The analysis of surface currents along with the inferred oil spill by the different satellites revealed that the northern part of the spilled oil moved under the influence of a mesoscale CE centered around 38°E, 20.75°N, and the southern part of the spilled oil was transported by the strong eastward currents of an anti-cyclonic eddy.

This study demonstrates the effective use of multi-mission satellite optical sensors to detect and track an oil spill incident in the Red Sea in the absence of SAR images. Though the low-resolution MODIS and Meteosat optical images could not efficiently detect the oil near the coastal areas, the high-resolution PlanetScope images completed the picture by providing 3 m resolution images near the coast, which allowed us to monitor the propagation of the oil slick near the Jeddah coast.

Detecting oil spills from satellite imagery using deep learning methods is currently an active field of research (e.g., [34,35,62–65]). These are expected to not only improve the detection of oil patches, but also help to diagnose the relative contributions of their forcing factors, such as wind and currents [4]. Future research will examine such artificial intelligence techniques to more efficiently merge information from multiple satellites, and to reduce the false alarm rates of oil spills. In addition, implementing region-specific special algorithms to estimate the thickness of the oil from satellite images can help better assess the impact of oil spreading on the marine resources [36,37,40,42].

Author Contributions: K.V., H.P.D., S.L., S.E.M., S.S., K.A., S.D. and I.H. have contributed in writing and reviewing and editing the manuscript. Conceptualization, K.V., H.P.D. and I.H.; methodology, K.V.; software, K.V.; validation, K.V. and S.S.; formal analysis, K.V., H.P.D. and S.S.; investigation, K.V., H.P.D. and S.S.; resources, I.H.; data curation, S.D.; writing—original draft preparation, K.V., H.P.D. and S.S.; visualization, K.V.; supervision, H.P.D., S.S. and I.H.; project administration, I.H.; funding acquisition, I.H. All authors have read and agreed to the published version of the manuscript.

Funding: This research and the APC was funded by Saudi ARAMCO under the project “An Intelligent Early-Warning Oil Spill Detection and Prediction System for the Arabian Gulf and the Red Sea” (grant number RGC/3/4290-01-01) and by the Vice President of Research Office at King Abdullah University of Science and Technology (KAUST) under the “Virtual Red Sea Initiative” (grant number REP/1/3268-01-01).

Data Availability Statement: Not applicable.

Acknowledgments: Sentinel-1/2, MODIS, Landsat-8 data, and Meteosat datasets were respectively acquired from ESA (<https://scihub.copernicus.eu/>), NASA (<https://modis.gsfc.nasa.gov/data/>), USGS (<https://www.usgs.gov/>), and EUMETSAT (<https://www.eumetsat.int/eumetsat-data-centre>). All four of these websites were accessed on 16 August 2020.

Conflicts of Interest: The authors declare no conflict of interest.

References

1. De Moura, N.V.A.; de Carvalho, O.L.F.; Gomes, R.A.T.; Guimarães, R.F.; de Carvalho Júnior, O.A. Deep-water oil-spill monitoring and recurrence analysis in the Brazilian territory using Sentinel-1 time series and deep learning. *Int. J. Appl. Earth Obs. Geoinf.* **2022**, *107*, 102695. [[CrossRef](#)]
2. Fartoosi, F.M.; Fartoosi, A.; Fartoosi, F.M.; Fartoosi, A. The Impact of Maritime Oil Pollution in the Marine Environment: Case Study of Maritime Oil Pollution in the Navigational Channel of Shatt Al-Arab. 2013. Available online: https://commons.wmu.se/all_dissertations/318/ (accessed on 21 October 2020).
3. iTop Federation. Oil Tanker Spill Statistics 2019. Available online: <https://www.itopf.org/knowledge-resources/data-statistics/statistics/> (accessed on 24 June 2021).
4. Al-Ruzouq, R.; Gibril, M.B.A.; Shanableh, A.; Kais, A.; Hamed, O.; Al-Mansoori, S.; Khalil, M.A. Sensors, features, and machine learning for oil spill detection and monitoring: A review. *Remote Sens.* **2020**, *12*, 3338. [[CrossRef](#)]
5. Hoteit, I.; Abualnaja, Y.; Afzal, S.; Ait-El-Fquih, B.; Akylas, T.; Antony, C.; Dawson, C.; Asfahani, K.; Brewin, R.J.; Cavalieri, L.; et al. Towards an end-to-end analysis and prediction system for weather, climate, and Marine applications in the Red Sea. *Bull. Am. Meteorol. Soc.* **2021**, *102*, E99–E122. [[CrossRef](#)]
6. Essa, S.; Harahsheh, H.; Shiobara, M.; Nishidai, T. Operational remote sensing for the detection and monitoring of oil pollution in the Arabian gulf: Case studies from the United Arab Emirates. *Dev. Earth Environ. Sci.* **2005**, *3*, 31–48.
7. Zodiatis, G.; Lardner, R.; Spanoudaki, K.; Sofianos, S.; Radhakrishnan, H.; Coppini, G.; Liubartseva, S.; Kampanis, N.; Krokos, G.; Hoteit, I.; et al. Operational oil spill modelling assessments. In *Marine Hydrocarbon Spill Assessments*; Elsevier: Amsterdam, The Netherlands, 2021; pp. 145–197.
8. El-Magd, I.A.; Zakzouk, M.; Abdulaziz, A.M.; Ali, E.M. The potentiality of operational mapping of oil pollution in the mediterranean sea near the entrance of the Suez canal using sentinel-1 SAR data. *Remote Sens.* **2020**, *12*, 1352. [[CrossRef](#)]
9. Huynh, B.Q.; Kwong, L.H.; Kiang, M.V.; Chin, E.T.; Mohareb, A.M.; Jumaan, A.O.; Basu, S.; Geldsetzer, P.; Karaki, F.M.; Rehkopp, D.H. Public health impacts of an imminent Red Sea oil spill. *Nat. Sustain.* **2021**, *4*, 1084–1091. [[CrossRef](#)] [[PubMed](#)]
10. Mittal, H.V.R.; Langodan, S.; Zhan, P.; Li, S.; Knio, O.; Hoteit, I. Hazard assessment of oil spills along the main shipping lane in the Red Sea. *Sci. Rep.* **2021**, *11*, 17078. [[CrossRef](#)] [[PubMed](#)]
11. Gianinetto, M.; Maianti, P.; Tortini, R.; Nodari, F.; Lechi, G. Evaluation of MODIS data for mapping oil slicks—the Deepwater Horizon oil spill case. In *Geographic Technologies Applied to Marine Spatial Planning and Integrated Coastal Zone Management*; Universidade Dos Açores: Ponta Delgada, Portugal, 2010; pp. 61–67.
12. Nukapothula, S.; Wu, J.; Chen, C.; Ali, P.Y. Potential impact of the extensive oil spill on primary productivity in the Red Sea waters. *Cont. Shelf Res.* **2021**, *222*, 104437. [[CrossRef](#)]
13. Li, Y.; Cui, C.; Liu, Z.; Liu, B.; Xu, J.; Zhu, X.; Hou, Y. Detection and monitoring of oil spills using moderate/high-resolution remote sensing images. *Arch. Environ. Contam. Toxicol.* **2017**, *73*, 154–169. [[CrossRef](#)] [[PubMed](#)]
14. Arslan, N. Assessment of oil spills using Sentinel 1 C-band SAR and Landsat 8 multispectral sensors. *Environ. Monit. Assess.* **2018**, *190*, 637. [[CrossRef](#)]
15. Jha, M.N.; Levy, J.; Gao, Y. Advances in remote sensing for oil spill disaster management: State-of-the-art sensors technology for oil spill surveillance. *Sensors* **2008**, *8*, 236–255. [[CrossRef](#)] [[PubMed](#)]
16. Leifer, I.; Lehr, W.J.; Simecek-Beatty, D.; Bradley, E.; Clark, R.; Dennison, P.; Hu, Y.; Matheson, S.; Jones, C.E.; Holt, B.; et al. State of the art satellite and airborne marine oil spill remote sensing: Application to the BP Deepwater Horizon oil spill. *Remote Sens. Environ.* **2012**, *124*, 185–209. [[CrossRef](#)]
17. Sun, S.; Hu, C.; Garcia-Pineda, O.; Kourafalou, V.; Le Hénaff, M.; Androulidakis, Y. Remote sensing assessment of oil spills near a damaged platform in the Gulf of Mexico. *Mar. Pollut. Bull.* **2018**, *136*, 141–151. [[CrossRef](#)]
18. Maianti, P.; Rusmini, M.; Tortini, R.; Dalla Via, G.; Frassy, F.; Marchesi, A.; Rota Nodari, F.; Gianinetto, M. Monitoring large oil slick dynamics with moderate resolution multispectral satellite data. *Nat. Hazards* **2014**, *73*, 473–492. [[CrossRef](#)]
19. Della Torre, C.; Tornambè, A.; Cappello, S.; Mariottini, M.; Perra, G.; Giuliani, S.; Amato, E.; Falugi, C.; Crisari, A.; Yakimov, M.M.; et al. Modulation of CYP1A and genotoxic effects in European seabass (*Dicentrarchus labrax*) exposed to weathered oil: A mesocosm study. *Mar. Environ. Res.* **2012**, *76*, 48–55. [[CrossRef](#)] [[PubMed](#)]
20. Ivanov, A.; He, M.; Fang, M. Oil spill detection with the RADARSAT SAR in the waters of the Yellow and East China Sea: A case study. In Proceedings of the 23rd Asian Conference on Remote Sensing, Kathmandu, Nepal, 25–29 November 2002.
21. Keramea, P.; Spanoudaki, K.; Zodiatis, G.; Gikas, G.; Sylaios, G. Oil spill modeling: A critical review on current trends, perspectives, and challenges. *J. Mar. Sci. Eng.* **2021**, *9*, 181. [[CrossRef](#)]
22. Kolokoussis, P.; Karathanassi, V. Oil spill detection and mapping using sentinel 2 imagery. *J. Mar. Sci. Eng.* **2018**, *6*, 4. [[CrossRef](#)]
23. Nezhad, M.M.; Croppi, D.; Marzialetti, P.; Piras, G.; Laneve, G. Mapping sea water surface in Persian Gulf, oil spill detection using Sentinel-1 images. In Proceedings of the 4th World Congress on New Technologies, Madrid, Spain, 19–21 August; 2018; pp. 19–21.
24. Rajendran, S.; Vethamony, P.; Sadooni, F.N.; Al-Kuwari, H.A.S.; Al-Khayat, J.A.; Govil, H.; Nasir, S. Sentinel-2 image transformation methods for mapping oil spill—A case study with Wakashio oil spill in the Indian Ocean, off Mauritius. *MethodsX* **2021**, *8*, 101327. [[CrossRef](#)]

25. Marghany, M.; Cracknell, A.P.; Hashim, M. Modification of fractal algorithm for oil spill detection from RADARSAT-1 SAR data. *Int. J. Appl. Earth Obs. Geoinf.* **2009**, *11*, 96–102. [CrossRef]
26. Guo, Y.; Zhang, H.Z. Oil spill detection using synthetic aperture radar images and feature selection in shape space. *Int. J. Appl. Earth Obs. Geoinf.* **2014**, *30*, 146–157. [CrossRef]
27. Fingas, M.; Brown, C.E. A review of oil spill remote sensing. *Sensors* **2018**, *18*, 91. [CrossRef] [PubMed]
28. Fingas, M.; Brown, C. Review of oil spill remote sensing. *Mar. Pollut. Bull.* **2014**, *83*, 9–23. [CrossRef] [PubMed]
29. Fingas, M.; Brown, C.E. *Oil Spill Remote Sensing: A Review*. *Oil Spill Science and Technology*; Gulf Professional Publishing: Boston, MA, USA, 2011; pp. 111–169.
30. Hu, C.; Li, X.; Pichel, W.G. Detection of Oil Slicks using MODIS and SAR Imagery. *IOCCG Rep.* **2006**, *5*, 14.
31. Zhao, J.; Temimi, M.; Ghedira, H.; Hu, C. Exploring the potential of optical remote sensing for oil spill detection in shallow coastal waters—a case study in the Arabian Gulf. *Opt. Express* **2014**, *22*, 13755. [CrossRef]
32. Times, Iran Says Oil Tanker Hit by Two Missiles off SAUDI Arabia Coast | Financial. Available online: <https://www.ft.com/content/2ae8d55a-ebef-11e9-a240-3b065ef5fc55> (accessed on 24 December 2021).
33. National, T. Iran Claims Oil Tanker Attacked in the Red Sea. Available online: <https://www.thenationalnews.com/world/mena/iran-claims-oil-tanker-attacked-in-the-red-sea-1.922005> (accessed on 24 December 2021).
34. Yekeen, S.T.; Balogun, A.L. Advances in remote sensing technology, machine learning and deep learning for marine oil spill detection, prediction, and vulnerability assessment. *Remote Sens.* **2020**, *12*, 3416. [CrossRef]
35. Yang, Y.J.; Singha, S.; Mayerle, R. A deep learning based oil spill detector using Sentinel-1 SAR imagery. *Int. J. Remote Sens.* **2022**, *43*, 4287–4314. [CrossRef]
36. Alpers, W.; Holt, B.; Zeng, K. Oil spill detection by imaging radars: Challenges and pitfalls. *Remote Sens. Environ.* **2017**, *201*, 133–147. [CrossRef]
37. Dong, Y.; Liu, Y.; Hu, C.; MacDonald, I.R.; Lu, Y. Chronic oiling in global oceans. *Science* **2022**, *376*, 1300–1304. [CrossRef]
38. Filipponi, F. Sentinel-1 GRD Preprocessing Workflow. *Proceedings* **2019**, *18*, 11.
39. Topouzelis, K.N. Oil spill detection by SAR images: Dark formation detection, feature extraction and classification algorithms. *Sensors* **2008**, *8*, 6642–6659. [CrossRef]
40. Rajendran, S.; Vethamony, P.; Sadooni, F.N.; Al-Kuwari, H.A.S.; Al-Khayat, J.A.; Seegobin, V.O.; Govil, H.; Nasir, S. Detection of Wakashio oil spill off Mauritius using Sentinel-1 and 2 data: Capability of sensors, image transformation methods, and mapping. *Environ. Pollut.* **2021**, *274*, 116618. [CrossRef] [PubMed]
41. Brekke, C.; Solberg, A.H.S. Oil spill detection by satellite remote sensing. *Remote Sens. Environ.* **2005**, *95*, 1–13. [CrossRef]
42. Garcia-Pineda, O.; Staples, G.; Jones, C.E.; Hu, C.; Holt, B.; Kourafalou, V.; Graettinger, G.; DiPinto, L.; Ramirez, E.; Streett, D.; et al. Classification of oil spill by thicknesses using multiple remote sensors. *Remote Sens. Environ.* **2020**, *236*, 111421. [CrossRef]
43. Moskolai, W.R.; Abdou, W.; Dipanda, A. A Workflow for Collecting and Preprocessing Sentinel-1 Images for Time Series Prediction Suitable for Deep Learning Algorithms. *Geomatics* **2022**, *2*, 435–456. [CrossRef]
44. Caballero, I.; Román, A.; Tovar-Sánchez, A.; Navarro, G. Water quality monitoring with Sentinel-2 and Landsat-8 satellites during the 2021 volcanic eruption in La Palma (Canary Islands). *Sci. Total Environ.* **2022**, *822*, 153433. [CrossRef] [PubMed]
45. Sanikommu, S.; Toye, H.; Zhan, P.; Langodan, S.; Krokos, G.; Knio, O.; Hoteit, I. Impact of atmospheric and model physics perturbations on a high-resolution ensemble data assimilation system of the Red Sea. *J. Geophys. Res. Oceans* **2020**, *125*, 8. [CrossRef]
46. Sanikommu, S.; Banerjee, D.S.; Baduru, B.; Paul, B.; Paul, A.; Chakraborty, K.; Hoteit, I. Impact of dynamical representational errors on an Indian Ocean ensemble data assimilation system. *Q. J. R. Meteorol. Soc.* **2019**, *145*, 3680–3691. [CrossRef]
47. Sanikommu, S.R.; Langodan, S.; Dasari, H.P.; Zhan, P.; Krokos, G.; Abualnaja, Y.O.; Asfahani, K.; Hoteit, I. Making the case for high resolution regional reanalyses: An example with the Red Sea. *Bull. Am. Meteorol. Soc.* **2022**; under review.
48. Toye, H.; Sanikommu, S.; Raboudi, N.F.; Hoteit, I. A hybrid ensemble adjustment Kalman filter based high-resolution data assimilation system for the Red Sea: Implementation and evaluation. *Q. J. R. Meteorol. Soc.* **2020**, *146*, 4108–4130. [CrossRef]
49. Klemas, V. Tracking oil slicks and predicting their trajectories using remote sensors and models: Case studies of the Sea Princess and Deepwater Horizon oil spills. *J. Coast. Res.* **2010**, *265*, 789–797. [CrossRef]
50. Pan, Q.; Yu, H.; Daling, P.S.; Zhang, Y.; Reed, M.; Wang, Z.; Li, Y.; Wang, X.; Wu, L.; Zhang, Z.; et al. Fate and behavior of Sanchi oil spill transported by the Kuroshio during January–February 2018. *Mar. Pollut. Bull.* **2020**, *152*, 110917. [CrossRef]
51. Rao, V.T.; Suneel, V.; Alex, M.J.; Gurumoorthi, K.; Thomas, A.P. Assessment of MV Wakashio oil spill off Mauritius, Indian Ocean through satellite imagery: A case study. *J. Earth Syst. Sci.* **2022**, *131*, 21. [CrossRef]
52. Patzert, W.C. Wind-induced reversal in Red Sea circulation. *Deep Sea Res. Oceanogr. Abstr.* **1974**, *21*, 109–121. [CrossRef]
53. Patlakas, P.; Stathopoulos, C.; Flocas, H.; Kalogeris, C.; Kallos, G. Regional climatic features of the Arabian Peninsula. *Atmosphere* **2019**, *10*, 220. [CrossRef]
54. Alharbi, F.R.; Csala, D. Gulf cooperation council countries' climate change mitigation challenges and exploration of solar and wind energy resource potential. *Appl. Sci.* **2021**, *11*, 2648. [CrossRef]
55. Sofianos, S.S.; Johns, W.E. An Oceanic General Circulation Model (OGCM) investigation of the red sea circulation: 2. Three-dimensional circulation in the Red Sea. *J. Geophys. Res. Oceans* **2003**, *108*, 1–15. [CrossRef]
56. Yao, F.; Hoteit, I.; Pratt, L.J.; Bower, A.S.; Köhl, A.; Gopalakrishnan, G.; Rivas, D. Seasonal overturning circulation in the Red Sea: 2. Winter circulation. *J. Geophys. Res. Oceans* **2014**, *119*, 2238–2262. [CrossRef]

57. Zhai, P.; Pratt, L.J.; Bower, A. On the crossover of boundary currents in an idealized model of the Red sea. *J. Phys. Oceanogr.* **2015**, *45*, 1410–1425. [[CrossRef](#)]
58. Bower, A.S.; Farrar, J.T. *Air–Sea Interaction and Horizontal Circulation in the Red Sea*; Springer Earth System Sciences; Springer: Berlin/Heidelberg, Germany, 2015; pp. 329–342.
59. Zhan, P.; Gopalakrishnan, G.; Subramanian, A.C.; Guo, D.; Hoteit, I. Sensitivity Studies of the Red Sea Eddies Using Adjoint Method. *J. Geophys. Res. Oceans* **2018**, *123*, 8329–8345. [[CrossRef](#)]
60. Zhai, P.; Bower, A. The response of the Red Sea to a strong wind jet near the Tokar Gap in summer. *J. Geophys. Res. Oceans* **2013**, *118*, 421–434. [[CrossRef](#)]
61. Zhan, P.; Subramanian, A.C.; Yao, F.; Kartadikaria, A.R.; Guo, D.; Hoteit, I. The eddy kinetic energy budget in the Red Sea. *J. Geophys. Res. Oceans* **2016**, *121*, 4732–4747. [[CrossRef](#)]
62. Krestenitis, M.; Orfanidis, G.; Ioannidis, K.; Avgerinakis, K.; Vrochidis, S.; Kompatsiaris, I. Oil spill identification from satellite images using deep neural networks. *Remote Sens.* **2019**, *11*, 1762. [[CrossRef](#)]
63. Li, B.; Xu, J.; Pan, X.; Ma, L.; Zhao, Z.; Chen, R.; Liu, Q.; Wang, H. Marine Oil Spill Detection with X-Band Shipborne Radar Using GLCM, SVM and FCM. *Remote Sens.* **2022**, *14*, 3715. [[CrossRef](#)]
64. De Kerf, T.; Gladines, J.; Sels, S.; Vanlanduit, S. Oil spill detection using machine learning and infrared images. *Remote Sens.* **2020**, *12*, 4090. [[CrossRef](#)]
65. Shaban, M.; Salim, R.; Khalifeh, H.A.; Khelifi, A.; Shalaby, A.; El-Mashad, S.; Mahmoud, A.; Ghazal, M.; El-Baz, A. A deep-learning framework for the detection of oil spills from SAR data. *Sensors* **2021**, *21*, 2351. [[CrossRef](#)] [[PubMed](#)]

Disclaimer/Publisher’s Note: The statements, opinions and data contained in all publications are solely those of the individual author(s) and contributor(s) and not of MDPI and/or the editor(s). MDPI and/or the editor(s) disclaim responsibility for any injury to people or property resulting from any ideas, methods, instructions or products referred to in the content.